Nanoscale

Accepted Manuscript

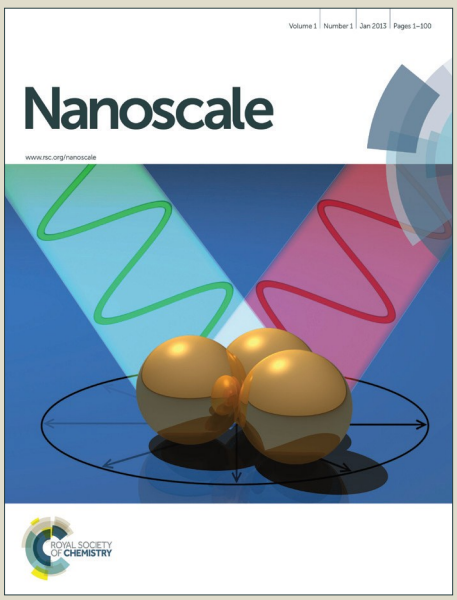

ROYAL SOCIETY OF CHEMISTRY

www.rsc.org/nanoscale

Journal Name

ARTICLE TYPE

Cite this: DOI: 10.1039/xxxxxxxxxx

Interaction grand potential between calcium-silicate-hydrate nanoparticles at the molecular level†

Patrick A. Bonnaud,*[a] Christophe Labbez,[b‡] Ryuji Miura,[a] Ai Suzuki,[a] Naoto Miyamoto,[a] Nozomu Hatakeyama,[a] Akira Miyamoto,[a] and Krystyn J. Van Vliet[c]

Received Date
Accepted Date

DOI: 10.1039/xxxxxxxxxx

www.rsc.org/journalname

Calcium-Silicate-Hydrate (or C-S-H), an inosilicate, is the major binding phase in cement pastes and concretes and a porous hydrated material made up of a percolated and dense network of cristalline nanoparticles of mean apparent spherical diameter ∼5 nm that are each stacks of multiple C-S-H layers. Interaction forces between these nanoparticles are at the origin of C-S-H chemical, physical, and mechanical properties at the meso- and macroscales. These particle interactions and resulting properties may be affected significantly by nanoparticle density and environmental conditions such as temperature, relative humidity, or concentration of chemical species in the bulk solution. In this study, we combined grand canonical Monte Carlo simulations and an extension of the mean force integration method to derive the pair potentials. This approach enables realistic simulation of the physical environment surrounding the C-S-H particles. We thus constructed the pair potentials for C-S-H nanoparticles of defined chemical stoichiometry at 10% relative humidity (RH), varying the relative crystallographic orientations at a constant particle density of $\rho_{\text{part}} \sim 2.21$ mmol/L. We found that cohesion between nanoparticles is affected strongly by both the aspect ratio and crystallographic misorientation of interacting particles. This method and findings underscore the importance of accounting for relative dimensions and orientation among C-S-H nanoparticles in descriptions of physical and simulated multiparticle aggregates or mesoscale systems.

1 Introduction

Although one typically views concrete structures as massive, macroscale components of the built infrastructure, the key binding phase of this chemically complex, composite material is comprised of nanoscale particles[1–3] of which calcium-silicate-hydrate (or C-S-H with C = CaO; S = SiO_2; H = H_2O) represents ∼60 vol% of the final product. As the production of this ubiquitous material also contributes 5-7% of CO_2 global emissions[4], there exists high motivation to improve its chemical and mechanical durability[3]. C-S-H being the major binding phase of hydrated cement and also the weakest[5], this phase is thus critical to cohesion and to physical and mechanical properties at meso- and macroscales[6–8].

C-S-H nanoparticles nucleate and grow during cement hydration from a supersaturated solution produced by the dissolution of cement clinker when mixed with water[1,9,10]; for the most widely used formulations, the ratio of Ca to Si is ∼1.7[11]. At the nanoscale, C-S-H layers have an inosilicate-type molecular structure[12,13] and aggregate to form nanoplatelet particles of 5-50 nm in apparent width that are charged and geometrically anisotropic[1,14–16]. Small Angle Neutron Scattering (SANS) experiments on hydrated cement samples indicated crystal coherence lengths of the order of few nanometers[15,17,18]. Strong cohesive forces between C-S-H nanoparticles (mainly electrostatic forces) facilitate nanoparticle aggregation, resulting in a mesoscale phase of apparent disorder[19,20]. As a consequence, hydrated cement pastes exhibit a multiscaled, porous network. Although complex and not completely understood, the mechanical and physical properties of cement and concrete depend directly on those of this C-S-H nanogranular phase. To date, mesoscale models of C-S-H as a colloidal system have adopted rather simplistic interparticle interaction models from the primitive model to ad-hoc potentials[21–25], and do not capture key features anticipated to contribute strongly to interactions among nanoscale hydrated particles at sub-nanometer interaction distances. Thus,

[a] Miyamoto Laboratory, New Industry Creation Hatchery Center, Tohoku University, Sendai, Miyagi, Japan. Fax: +81 22 795 7235; Tel: +81 22 795 7233; E-mail: patrick@aki.niche.tohoku.ac.jp
[b] Laboratoire Interdisciplinaire Carnot de Bourgogne, UMR 6303, CNRS - Univ. Bourgogne Franche-Comté, F-21078, Dijon, France.
[c] Department of Materials Science and Engineering, Massachusetts Institute of Technology, Cambridge, MA 02139, USA.

† Electronic Supplementary Information (ESI) available: [details of any supplementary information available should be included here]. See DOI: 10.1039/b000000x/

quantitative understanding of aggregation forces acting among C-S-H nanoparticles is of primary importance in the challenging quest to predict and improve properties of the hydrated material.

Generally, interparticle forces can be quantified experimentally by the surface force apparatus (SFA) or atomic force microscope (AFM)-based force spectroscopy; and inferred from Small Angle Scattering (SAS) measurements of particle dispersions. These experimental approaches have provided valuable insights for the effects of environment and composition for interacting surfaces of specific geometries[26–28] and for weak-to-moderate cohesion forces[7,27], but are both more challenging and less informative for analysis of C-S-H nanoparticles that are characterized by nanoscale and anisotropic dimensions, strong interactions, and volume fraction dependence. For the particular case of C-S-H nanoparticles of finite surface charge, the molecular nature of the confined fluid is important over distances of $<$1 nm. In such cases that are less amenable to experiment, molecular and mesoscale simulations can provide valuable, quantitative information about aggregation forces.

Interactions between charged particles are described classically with the DLVO theory[29], a theory developed at the level of the mean field approximation, where particles are structureless with a surface charge density compensated by ions defined as point charges, surrounded by a solvent (e.g., water) described as a continuum, and interacting between each others and with the particles via a mean field[29]. The DLVO theory assumes that the interactions are a superposition of electrostatic forces as described by the linearized Poisson-Boltzmann equation and dispersion or van der Waals forces. In such theory, the pair potential is supposed independent of the particle density[30], making this approach invalid for dense particle dispersions[31]. Indeed, the surrounding solution (solvent and ions) is always under the influence of electric fields generated by particles (colloids), and thus the equilibrium concentrations (those of the reservoir) are not realized. Therefore, the Debye screening length λ_D (i.e., the range of electrostatic forces) is not only a function of the reservoir ionic concentrations but also a function of the particle volume fraction ϕ. On this basis, Beresford-Smith and Chan[32] and Trizac et al.[33] developed ϕ-dependent pair potential between charged isotropic particles and charged anisotropic particles, but stayed limited to weak coupling regime (low surface charge density, low volume fractions, low ionic concentrations, and monovalent counterions). Only recently, one of us[34] introduced a new method based on mesoscopic simulations at the level of the full primitive model (an extension of the DLVO theory where ions have a width of the ionic radius plus the first solvation shell and can move independently[19,35,36]). We showed that, in the strong coupling regime, the cohesion forces or correlation forces are strengthened when ϕ is increased. The method allows the determination of pair potential even when ionic correlations are important (strong coupling regime) and for non-spherical particles and heterogeneous charge distributions. Although the method developed in Ref. 34 is well suited to molecular simulations, it has so far only been applied at the level of the primitive model. The molecular nature of the solvent (discrete water molecules and ions), which can contribute strongly at short interparticle distances ($<$1 nm) was thus not considered. While only a few molecular simulation works tackle the problem of the effect of the molecular nature of water on interaction forces between particles at finite concentrations (for neutral silica[37–39] or clay[40,41] particles), to our knowledge there is no such work for C-S-H nanoparticles. In other words, the cohesion forces at short distances ($<$1 nm, where the molecular nature of the solvent is important), and the dependence of these on ϕ, are not yet known for cement despite its widespread use.

On the basis of our previous work at the molecular scale on calcium-silicate-hydrate cohesion at ambient[42] and high temperatures[43], we employ in this paper computational modeling and molecular simulation to explore potentials and forces between calcium-silicate-hydrate nanoparticles mediated by aqueous solutions at a molecular level. We use this approach to consider effects of geometric and crystallographic anisotropy at room temperature (300 K), low relative humidity (10%RH), and particle density of $\rho_{\text{part}} \sim 2.21$ mmol/L (i.e., a particle volume fraction of $\phi \sim 0.06$). We present the methods used to build our molecular models and to simulate our systems, and then to calculate interaction grand potential (or interaction Landau free energy) between calcium-silicate-hydrate particles at low humidities. These findings and approaches will also enable future construction of interaction grand potential for higher humidities, varying C-S-H chemical compositions, and other environmental conditions of interest.

2 Methods

2.1 Building molecular models for C-S-H particles

The molecular model we designed draws on the previously reported molecular structure of calcium-silicate-hydrates as a basic unit[44]. This model has been used by some of us to simulate water content within individual calcium-silicate-hydrate nanoparticles[42,45] and also C-S-H nanoscale slit pores[42,43]. Note that in the remainder of this paper we follow the notation in cement chemistry to denote CaO as C, SiO_2 as S, and H_2O as H, such that calcium-silicate-hydrate is termed simply C-S-H. In this molecular model of C-S-H, two silicate-rich layers are explicitly described in the simulation box. The calcium-to-silicon ratio of this structure is C/S = 1.65, similar to the mean value found using energy dispersive X-ray analysis[46,47] of hardened Portland cement pastes (C/S=1.70). Surface charge of this C-S-H molecular structure arises from ionized silanol groups in the silica chains; we used the PN-TrAZ force field published elsewhere[42] to reflect this with σ=-0.73 C.m^{-2}. The surface charge is compensated with calcium counterions to maintain system electroneutrality. The original molecular model was enclosed in a triclinic box of $(a,b,c) = (1.33$ nm, 2.95 nm, 2.37 nm) with angles $(\alpha,\beta,\gamma) = (92.02°$, 88.52°, 123.58°). We did not further equilibrate the unit cell of this previously validated structure, before constructing single particles and then pairs of particles within a simulated water box; all equilibration was constructed in a GCMC framework on the systems comprising particle pairs and water at the specified relative humidity. Note that the subscript 'w' was added to atoms and ions belonging to the fluid so that (i) oxygen atoms and hydrogen atoms of

water molecules are labelled O_w and H_w, respectively; (*ii*) calcium counterions are labelled C_w. Silicon atoms, oxygen atoms, and calcium ions in the C-S-H molecular structure are labelled *Si*, *O*, and *Ca*, respectively. We called 'Particle' all atoms constituting the C-S-H molecular structure (i.e., *Si*, *O*, and *Ca*).

A single particle was first built by duplicating the aforementioned unit cell three times along the a direction (aligned with the cartesian axis x) and one time along the b direction (forming an angle of 33.58° with the cartesian axis y in the $\{O,x,y\}$ plan, O being the axis origin). Such number of duplicate unit cells was chosen to construct a particle of ∼5 nm in x and y directions, in agreement with previous experimental findings[15]. To form particles of finite dimensions, periodic boundary conditions were removed and thus some silicon bonds remain unsaturated; oxygen atoms were added to silica chains to resolve this. The resulting particle dimensions were $a_{\text{part}} \sim 5.32$ nm, $b_{\text{part}} \sim 5.9$ nm, and $c_{\text{part}} \sim 1.87$ nm (for c_{part}, 0.5 nm were removed from the original molecular structure as this corresponds roughly to the intrinsic pore width of the previous structure). The volume of the particle was thus $v_{\text{part}} \sim 49$ nm^3 and particle aspect ratios were b_{part}:$a_{\text{part}} \sim 1.1$ and c_{part}:$a_{\text{part}} \sim 0.3$.

Three different configurations of particle pairs were considered (Fig. 1): A, B, and C. To build configuration A, the particle was duplicated, and the second particle was translated along the c-axis by a distance of ∼6.36 nm between the centers of mass; this corresponded to ∼4 nm between opposing free surfaces. To build configuration B or C, the second particle was first rotated by 123.58° or 88.52° around the z or x cartesian axes, respectively, and then translated along the c-axis by ∼6.36 nm. Note that the resulting distance between opposing free surfaces in configuration C was ∼2.23 nm, due to the c_{part}:a_{part} particle aspect ratio of ∼0.3. Furthermore, unfilled space was added around particles by increasing the length of the simulation box by 6.6 nm, 6 nm, and 4 nm along the a, b and c directions, respectively; that space was subsequently filled with explicit water molecules at the corresponding temperature and humidity (of corresponding fugacity in grand canonical Monte Carlo simulations). Finally, particle pairs were enclosed in a triclinic box of $(a,b,c) = (11.92$ nm, 11.90 nm, 12.74 nm) with angles $(\alpha,\beta,\gamma) = (92.02°, 88.52°, 123.58°)$. Thus, the simulated system had a particle density of $\rho_{\text{part}} \sim 2.21$ mmol/L with a resulting volume fraction of $\phi \sim 0.06$. This particle density was low compared to that expected for hardened cement pastes[48] described as low density (LD) and high density (HD) C-S-H with $\phi_{\text{LD}} \sim 0.64$ and $\phi_{\text{HD}} \sim 0.74$, respectively. However, it is a first step in the exploration of the effect of volume fraction on mean forces and interaction grand potential at the molecular scale.

2.2 Interatomic Potential and Grand Canonical Monte Carlo simulations

We used a classical potential combining dispersion-repulsion interactions (short-range interactions) with electrostatic interactions (long-range interactions), to describe interactions among atoms in the C-S-H particles and between those atoms among explicit water molecules and calcium counterions. For dispersion-repulsion interactions, we employed the mathematical form used in the PN-TrAZ method[49] to derive dispersion parameters:

$$U_{ij}(r_{ij}) = A_{ij}\exp(-b_{ij}r_{ij}) - \sum_{n=3}^{5} f_{2n}(r_{ij})\frac{C_{2n}^{ij}}{r_{ij}^{2n}} \quad (1)$$

where r_{ij} is the distance between an atom i and an atom j, A_{ij} and b_{ij} are repulsive parameters, C_{2n}^{ij} are dispersion parameters and $f_{2n}(r_{ij})$ is a damping function to avoid divergence of the potential at very short range and defined as:

$$f_{2n}(r_{ij}) = 1 - \sum_{m=0}^{2n}\frac{(b_{ij}r_{ij})^m}{m!}\exp(-b_{ij}r_{ij}). \quad (2)$$

Ref. 42 provides full details of input parameters to derive dispersion parameters, as well as repulsion-dispersion parameters for water-C-S-H particle interactions and calcium ion-C-S-H particle interactions. For dispersion-repulsion interactions among atoms in C-S-H particles, parameters are reported in Table 1. All partial charges were taken from Ref. 42. For interactions between water molecules, we employed the rigid-SPC model[45,50] in order to simulate a large number of water molecules (N_{water} per simulation box > 2600 molecules) in a reasonable amount of time. In the course of the simulation, dispersion-repulsion interactions were summed within a cutoff radius of $R_{\text{cut}} \sim 1.5$ nm. The Ewald summation technique was employed to account for the long-range component of the electrostatic interactions with parameters $\kappa = 0.2$ Å^{-1} and $k_{\max} = 5$.

In this work, we seek to characterize the potential between C-S-H particle pairs in a given environment defined by temperature (T) and relative humidity (RH). A suitable computational framework for such conditions is the grand canonical Monte Carlo (GCMC) simulation, where the volume V of the system is constant and is in equilibrium with an infinite reservoir of water molecules of defined chemical potential μ_{water} and temperature T[51]. The chemical potential is related to the fugacity (pressure of the gas if it were an ideal gas) by $f_{\text{water}} = \exp(\beta\mu_{\text{water}})/\beta\Lambda_{\text{water}}^3$, where $\beta = 1/k_B T$, $\Lambda_{\text{water}} = \sqrt{\beta h^2/(2\pi m_{\text{water}})}$ is de Broglie thermal wavelength, h is Planck's constant, and m_{water} is mass of a water molecule. We consider here that C-S-H particles are in contact with a reservoir having a fugacity $f_{\text{water}} = 0.1P_0$, where P_0 is the saturating vapor pressure (the pressure at which for a given temperature we are at the bulk liquid-gas equilibrium). For the rigid-SPC water model, this pressure is P_0^{SPC} (T_0 = 300 K) = 4.4 kPa[52]. At room temperature ($T_0 = 300$ K) and for the value of the fugacity that we consider, we can assume that the pressure of the gas reservoir is $P_{\text{water}} = f_{\text{water}}$ (ideal gas), meaning that the chosen fugacity corresponds to a relative humidity (RH) of 10%, where RH = P_{water}/P_0. Only the number of water molecules was allowed to fluctuate in the simulation box, as the other species are treated in the canonical ensemble: they were allowed to move while their number was maintained constant to preserve system electroneutrality. Furthermore, silica chains within C-S-H particles were kept rigid in the course of the simulations, i.e., atomic positions of silcon atoms and oxygen atoms (those bonded to silicon atoms in C-S-H particles) in silica chains remained fixed. All other species including water molecules, calcium ions, and oxygen atoms in the ionic state were unconstrained and could thus

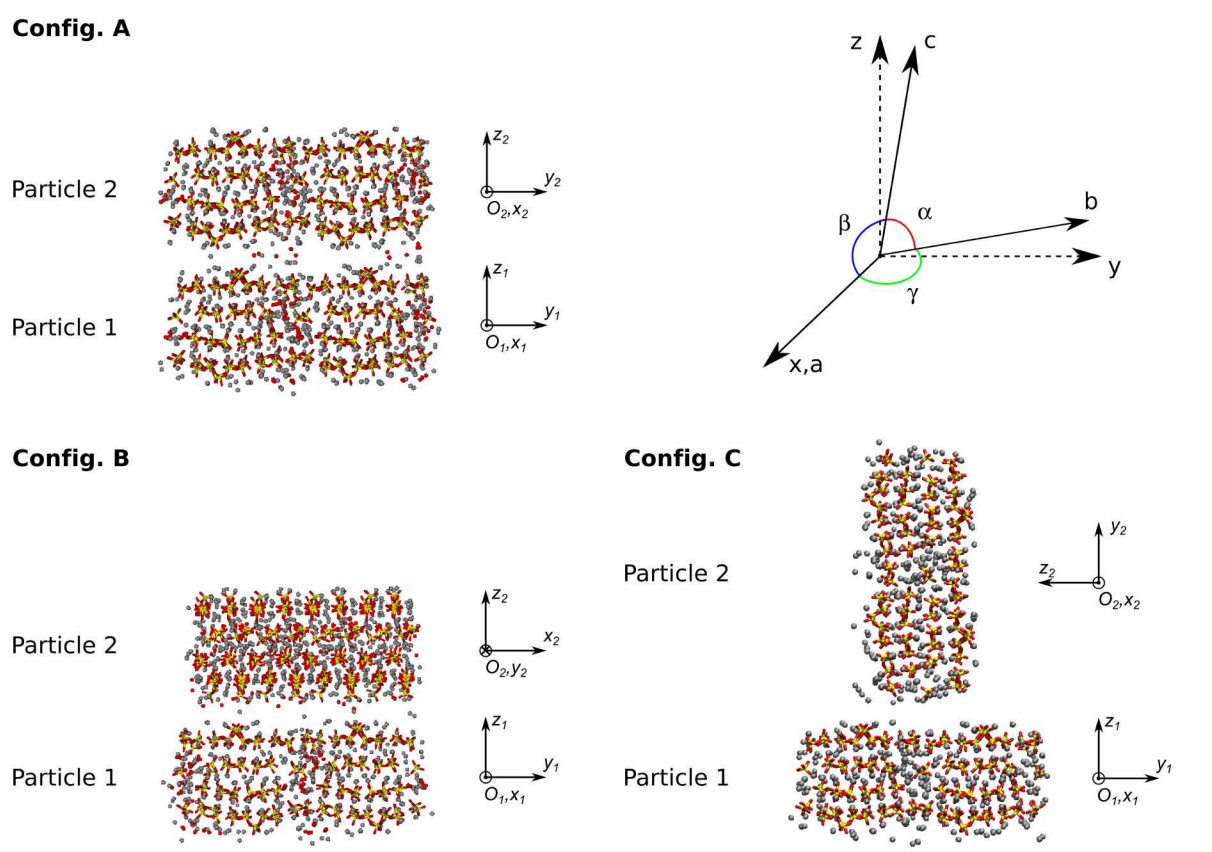

Fig. 1 Snapshots illustrating the three distinct orientational configurations of calcium-silicate-hydrate (C-S-H) particle pairs used to calculate interaction grand potential at the molecular level. Water molecules are removed for clarity. Red and yellow sticks represent silica chains, and gray spheres represent calcium ions in the molecular structure (Ca) and calcium counterions (C_w). For each configuration, the bottom particle (particle 1) is taken as the reference particle. Local cartesian axes guide the reader to visualize particle orientations with respect to centers of mass (O_1 for particle 1 and O_2 for particle 2). While x_1, y_1, z_1 are axes for particle 1, x_2, y_2, z_2 are axes for particle 2. $\odot$ is the symbol for an axis pointing toward the reader and $\otimes$ for an axis pointing away from the reader. Crystallographic triclinic axes a, b, and c are shown relative to the cartesian axes x, y, z. Configuration A refers to a configuration where the two interacting particles are parallel to each other and the silica chains are oriented in the same direction. Configuration B refers to a configuration where particle 2 has been rotated by $\sim$123.58° around the z-axis with respect to the reference particle 1. Configuration C refers to a configuration where particle 2 has been rotated by $\sim$88.52° around the x-axis with respect to the reference particle 1.

Table 1 Repulsion and dispersion parameters for interactions among atoms in the C-S-H particles obtained following PN-TrAZ method[49] with input parameters taken from Ref. 42.

C-S-H species 1	C-S-H species 2	C_6 [Ha.a_0^6]	C_8 [Ha.a_0^8]	C_{10} [Ha.a_0^{10}]	A [Ha]	b [a_0^{-1}]
Si	Si	3.0751	36.1851	556.6838	6163.4000	2.3950
O	O	38.2825	645.7175	14527.4019	1543.5000	2.1900
Ca	Ca	10.5740	209.4457	2404.4830	990.6686	2.3744
Si	O	10.8429	155.5211	2947.7701	3084.3489	2.2879
Si	Ca	5.4303	91.1302	1160.3969	2471.0092	2.3847
O	Ca	19.3615	368.0849	6782.4262	1236.5666	2.2785

relax during equilibration runs. This also means that C-S-H particles were not alllowed to translate or rotate in the course of simulations. Periodic boundary conditions were used along the a, b, and c directions, resulting in a finite particle density of $\rho_{\text{part}} \approx 2.21$ mmol/L. Finally, several GCMC runs of 400 million accepted steps were performed to reach equilibrium. Our criteria for equilibrium are a stable system energy (standard deviation of energy data $<2\times10^{-3}\%$ of the mean value) and a stable exchange of water molecules (the difference between the number of inserted water molecules and the number of removed water molecules within 5%). In our approach, we considered that we reached equilibrium when the last GCMC equilibration run fulfilled both criteria, prior to any data production run. At equilibrium, data were then recorded using a GCMC production run of 400 million accepted steps with a sampling of atomic configurations every 10,000 accepted steps.

2.3 Interaction grand potential

The ensemble of coordinates in the volume delimited by the simulation box is written as: $\{R\}$. In this work, we computed the interaction grand potential between C-S-H particles, i.e., the grand potential profile along a reaction coordinate $R' \in \{R\}$. Here, the reaction path is a straigth line passing through the center of mass R_1 of particle 1 (the fixed, reference particle) and collinear to the c-axis. The interaction grand potential is the grand potential of the system when the center of mass of particle 2, R_2, is on the reaction path (i.e., $R_2 = R'$). Note that instead of using R_1 and R_2, we considered the distance between centers of mass defined by $D = R_2 - R_1$. Then, when particle 2 is on the reaction path we used $D' = \delta(R' - R_2)D$ instead of R' (see Fig. 2). Furthermore, we defined the number of water molecules, the number of calcium counterions (C_w), and the number of atoms constituting C-S-H particles (Ca, O, and Si) by N_{water}, N_{C_w}, and $N_{\text{C-S-H}}$.

The grand canonical ensemble is defined here by μ_{water}, V, T. From a statistical mechanics point of view, the appropriate thermodynamic quantity to consider is the grand potential (or the Landau free energy) written as:

$$\Omega(\mu_{\text{water}}, N_{C_w}, N_{\text{C-S-H}}, V, T) = F(N_{\text{water}}, N_{C_w}, N_{\text{C-S-H}}, V, T) - \mu_{\text{water}} N_{\text{water}}, \quad (3)$$

where F is the Helmoltz free energy (i.e., the thermodynamic

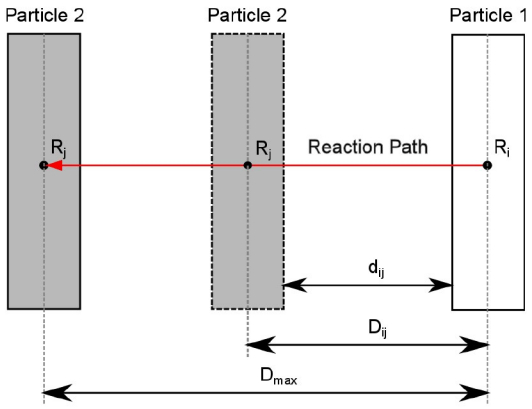

Fig. 2 Schematic showing the two interacting calcium-silicate-hydrate particles (black solid line, and black dashed line rectangles). Particle 1 is the reference particle and its fixed center of mass is the origin of the reaction path, R_i. Particle 2 is the particle that is moved for each simulation point in the computation of interaction grand potentials. Particle 2 follows the reaction path represented by a red arrow, to sample different interparticle distances. The location of particle 2 on the reaction path is defined by R_j and the distance between the centers of mass of the two interacting particles is defined by $D_{ij} = R_j - R_i$. d_{ij} is noted as the resulting distances between opposing free surfaces. $D_{\text{max}} \sim 6.36$ nm is the maximum distance between the particles considered herein.

potential related to the canonical ensemble); or equivalently as:

$$\Omega(\mu_{\text{water}}, N_{C_w}, N_{\text{C-S-H}}, V, T) = -\frac{1}{\beta}\ln\Xi(\mu_{\text{water}}, N_{C_w}, N_{\text{C-S-H}}, V, T). \quad (4)$$

$\Xi(\mu_{\text{water}}, N_{C_w}, N_{\text{C-S-H}}, V, T)$ is the Grand Partition function of the system. Note that in the remainder of the article we omitted the explicit N_{C_w} and $N_{\text{C-S-H}}$ dependence to simplify the notation. $\Xi(\mu_{\text{water}}, V, T)$ can be written as a sum over states s of the phase space including their related potential energy, U_s, and number of water molecules, N^s_{water}:

$$\Xi(\mu_{\text{water}}, V, T) = \sum_s \exp\left(-\beta(U_s - \mu_{\text{water}}N^s_{\text{water}})\right). \quad (5)$$

Consequently, the probability of finding the system in a state s is:

$$\pi_s = \frac{\exp(-\beta(U_s - \mu_{\text{water}}N^s_{\text{water}}))}{\Xi(\mu_{\text{water}}, V, T)}. \quad (6)$$

Similarly, the probability of finding particles at a particular value D' on the reaction path is:

$$\pi_s(D') = \frac{\delta(D' - D_s)\exp(-\beta(U_s - \mu_{\text{water}}N^s_{\text{water}}))}{\Xi(\mu_{\text{water}}, V, T)} = \pi_s\delta(D' - D_s). \quad (7)$$

Using eq. (7) and summing over states s of the phase space gives the reaction path probability:

$$P(D') = \sum_s \pi_s\delta(D' - D_s). \quad (8)$$

Equivalently, if one defines the D'-dependent Grand Partition function as,

$$\Xi(\mu_{\text{water}}, V, T, D') = \sum_s \delta(D' - D_s) \times \exp(-\beta(U_s(D') - \mu_{\text{water}}N^s_{\text{water}}(D'))), \quad (9)$$

we then have,

$$P(D') = \frac{\Xi(\mu_{\text{water}}, V, T, D')}{\Xi(\mu_{\text{water}}, V, T)}. \quad (10)$$

Rearranging eq. (10) and using eq. (4), the D'-dependent grand potential is:

$$\Omega(D') = -\frac{\ln P(D')}{\beta} - \frac{\ln\Xi(\mu_{\text{water}}, V, T)}{\beta}. \quad (11)$$

Deriving eq. (11) with respect to the interparticle distance D', we get:

$$\frac{\partial\Omega(D')}{\partial D'} = -\frac{1}{\beta}\frac{\frac{\partial P(D')}{\partial D'}}{P(D')} = \frac{1}{\Xi(\mu_{\text{water}}, V, T, D')} \times \sum_s \delta(D' - D_s)\left[\frac{\partial U_s(D')}{\partial D'} - \mu_{\text{water}}\frac{\partial N^s_{\text{water}}(D')}{\partial D'}\right] \times \exp(-\beta(U_s(D') - \mu_{\text{water}}N^s_{\text{water}}(D'))), \quad (12)$$

where $-\partial U_s(D')/\partial D' = f_s(D')$ is the force between the two interacting particles at distance D' on the reaction path and for state s. Then,

$$\frac{\partial\Omega(D')}{\partial D'} = -\langle f(D')\rangle_{D'} - \mu_{\text{water}}\left\langle\frac{\partial N_{\text{water}}(D')}{\partial D'}\right\rangle_{D'}. \quad (13)$$

Integrating eq. (13) from infinity to one specific interparticle distance D_{ij} between interacting C-S-H particles i and j, we finally obtained:

$$\Omega(D_{ij}) = -\int_\infty^{D_{ij}}\langle f(D')\rangle_{D'}\mathrm{d}D' - \mu_{\text{water}}\int_\infty^{D_{ij}}\left\langle\frac{\partial N_{\text{water}}(D')}{\partial D'}\right\rangle_{D'}\mathrm{d}D' + \Omega(\infty). \quad (14)$$

Eq. (14) constitutes the fundamental equation of mean force integration to obtain the interaction grand potential between two C-S-H particles. Note that eq. (14) is a modified version of the previously established mean force integration method in the canonical ensemble[53]. Here, each specific interparticle distance D_{ij} between interacting C-S-H particles i and j corresponds to one complete GCMC simulation. Incremental distances ΔD_{ij} between simulated points varied to enable increased sampling near the energetic transitions that occurred at lower D_{ij}, and are summarized in Table 2. We simulated up to 66 D_{ij} along the c-axis for each of the particle configurations considered (A, B, and C). Figure 2 illustrates the distances between particle centers of mass D_{ij} and particle opposing surfaces d_{ij} over these trajectories.

We used Refs. 54 and 42 to compute electrostatic (Ewald) and dispersion-repulsion (Lennard-Jones and PN-TrAZ) forces, respectively. We validated our algorithm against the DL_POLY Molecular Simulation Package (version 2.19)[55] by computing forces for a simple system of two interacting opposite charge ions (see Supporting Information). Furthermore, note that the first derivative of the interaction grand potential does not give forces between particles (see eq. (12)). Indeed, because of the use of the grand canonical ensemble a quantity related to the variation of the water content as a function of D_{ij} is also included in the interaction grand potential.

The present approach to construct the interaction grand potential necessitates the use of GCMC simulations, and thus requires more real time to complete simulations than other approaches that compute free energy profiles from classical molecular dynamics simulations. Ebrahimi et al. have recently suggested an MD-based approach for clay particles[41]. In the latter case, the code can be fully parallelized and thus computed free energies can be obtained more quickly than in GCMC. Full code parallelization is not straightforward and does not offer significant compute-time savings in GCMC, as computations follow the Markov chain. However, a key advantage of the present approach is that we accurately consider the effect of the environment, including exchange of water molecules and finite particle volume fractions, on the resulting energy profile. Furthermore, the effect of the particle volume fraction on energy profiles has long been considered an important component, noted in previous mesoscale simulations of particle aggregates[34]. Such effects are omitted from consideration in the MD-based free energy profile approach, such that particle configuration and volume fraction effects are con-

Table 2 Incremental distance (ΔD_{ij}) between interacting C-S-H particles i and j as a function of the interparticle distance (D_{ij}), where D_{ij} is defined as the distance between particle centers of mass.

Configuration	Interparticle distance D_{ij} [nm]	Incremental distance ΔD_{ij} [nm]
A and B	< 2.31	$\sim$0.01
	$2.31 < < 3.32$	$\sim$0.05
	$3.32 < < 4.33$	$\sim$0.10
	$4.33 < < 6.36$	$\sim$0.25
C	< 3.65	$\sim$0.01
	$3.65 < < 4.33$	$\sim$0.03
	$4.33 < < 5.00$	$\sim$0.07
	$5.00 < < 6.36$	$\sim$0.17

volved[41].

3 Results and discussion

C-S-H particles are reportedly anisotropic in geometry and crystallography. Interaction forces among particles may vary with respect to relative particle orientation, and such variations could then affect mechanical properties of cement pastes. We accounted for this effect by considering three particle-pair configurations that widely varied the relative crystallographic misorientation (Fig. 1). While configuration A represents two interacting particles aligned in parallel such that the silica chains are oriented in the same direction, configuration B refers to a configuration where the two interacting particles maintain the same opposing surface, but particle 2 is rotated in plane by $\sim$123.58° around the z-axis with respect to particle 1 (see Fig. 1), changing the relative orientation of silica chains in the two particles. In this way, configuration B explores the effect of silica chain misorientation, with the same surface-normal, on interaction grand potentials. Configuration C refers to a configuration where particle 2 is rotated by $\sim$88.52° around the x-axis with respect to particle 1 (see Fig. 1). In this configuration, the interacting surface of particle 2 is different, and the projected surface area of overlap is smaller than that in configurations A and B due to the particle aspect ratio of c_{part}:$a_{\text{part}} \sim 0.3$. Configuration C thus also explores the effect of the nature of interacting free surfaces (surface chemistry and topography) on the interaction grand potentials. Note that the cartesian coordinates used to define the relative particle orientation (x,y,z) are not exactly coincident with the crystallagraphic axes (a,b,c), as indicated in Fig. 1.

3.1 Water content and mean force between C-S-H particles

Figure 3 shows the excess number of water molecules $\Delta N_{\text{water}} = N_{\text{water}}(D_{ij}) - N_{\text{water}}(D_{\max})$ and the mean force $\langle f(D_{ij})\rangle$ as a function of the distance between C-S-H particle pairs for configurations A, B, and C ($D_{\max} = 6.36$ nm). The reference average number of water molecules $N_{\text{water}}(D_{\max})$ was 3276.3 (configuration A), 3336.8 (configuration B), and 3275.4 (configuration C). For each interparticle configuration considered, a maximum number of water molecules corresponded to the point at which this "condensed" water was maximized due to confinement effects between C-S-H particles (e.g., see the molecular configuration in Fig. 3d). This maximum N_{water} also corresponded to a minimum in potential energy (see Supporting Information). For configurations A and B, this maximum of water molecules occurred at the same distance D_{ij} between C-S-H particles ($D_{ij} \sim 3.16$ nm). The absolute number of water molecules in both configurations was similar ($N_{\text{water}} \sim 3550$ molecules). Configuration B was established to probe the effect of in-plane misorientation of the silicate-rich surfaces of the particle pairs. Here, we observed that this in-plane rotation between the particles negligibly affected the water content. For configuration C, the maximum number of water molecules occurred at larger separation distances, $D_{ij} \sim 4.87$ nm. This difference is attributable to the c_{part}:a_{part} particle aspect ratio that reduced the gap between particle pair surfaces d_{ij} for the same distance D_{ij} in configuration C. Indeed, insets in Figs. 3b-c show results as a function of d_{ij}, the distance between opposing free surfaces, to distinguish these effects. We observed that maxima in number of water molecules were similar among all particle pair configurations, and appeared in the range $0.65 < d_{ij} < 0.9$ nm, with the lowest distance being for the peak corresponding to configuration C. Note that negative values for d_{ij} were possible due to our definition of the location of free surfaces, which we defined by the furthest oxygen atom in silica chains with respect to the center of mass of the particle in each direction (a, b, and c). The absolute maximum number of water molecules in configuration C was similar to configurations A and B ($\sim$3550). Note that Leroch et al.[38] found a similar behavior of the water content between two silica particles (presence of a maximum in the average number of water molecules plotted as a function of D_{ij}).

Fig. 3b shows the mean force as a function of the distance between C-S-H particle pairs. Mean forces cancelled very close to simulation points located at $\sim$2.4 nm (configuration A), $\sim$2.45 nm (configuration B), and $\sim$3.92 nm (configuration C). Minima of mean forces were found at interparticle distances of $\sim$2.50 nm, $\sim$2.45 nm, and $\sim$3.99 nm, for configurations A, B, and C, respectively. Minima of mean forces were -24.34 nN (configuration A), -1.97 nN (configuration B), and -11.53 nN (configuration C). The absolute value of the previous quantity is often taken as the adhesion force[29]. Experimentally, Plassard et al.[7] measured an adhesion force of $F_{\text{adh}}^{\text{exp.}} = 60$ nN at $\sim$300 K and for 1%RH (dry air conditions) between C-S-H surfaces by Atomic Force Microscopy (AFM). Note that prior to compare our data with the previous experimental values, we checked with the help of a slit pore molecular model of a width of 4 nm that the water layer thickness at the C-S-H surface does not change significantly between roughly 1% and 10%RH at 300 K. We found an average thickness of $\sim$0.395 nm

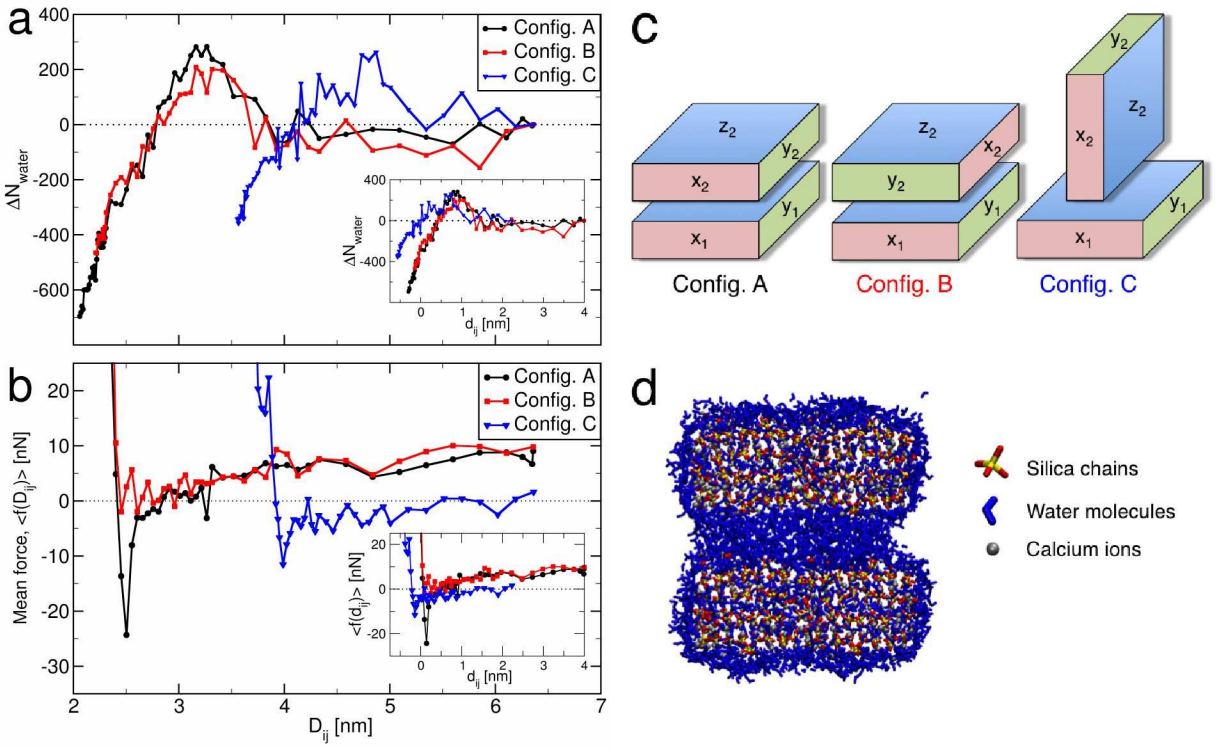

Fig. 3 (a) Excess number of water molecules $\Delta N_{\mathrm{water}} = N_{\mathrm{water}}(D_{ij}) - N_{\mathrm{water}}(D_{\mathrm{max}})$ and (b) mean force $\langle f(D_{ij})\rangle$ as a function of the distance D_{ij} between interacting calcium-silicate-hydrate particles ($D_{\mathrm{max}} = 6.36$ nm). Black filled circles, red filled squares, and blue filled down triangles correspond to configurations A, B, and C, respectively. Insets in a and b show results as a function of d_{ij}, the distance between opposing free surfaces. (c) Cartoons showing the calcium-silicate-hydrate (C-S-H) particle pairs in configurations A, B, and C. $\{x_1, y_1, z_1\}$ and $\{x_2, y_2, z_2\}$ refer to surface normals for particle 1 (bottom) and particle 2 (top), respectively. (d) Snapshot of a molecular structure in configuration A at an interparticle distance close to the maximum of water molecules ($D_{ij} \sim 3.16$ nm).

at 1.25%RH and ∼0.435 nm at 10%RH. The water layer thickness is on the order of a SPC water molecule (0.311 nm) and slightly varies between the two considered RH. Our simulation values for configurations A and C are of the same order of magnitude with respect to the experimental value of Plassard et al., while our simulation value for configuration B is one order of magnitude lower. Since, the adhesion force is strongly dependent on the interacting surface, a direct comparison is not necessarily the most relevant. Plassard et al.[7] also computed the force per unit area and found $F^{\text{exp.}}_{/\text{area unit}} \sim 9.28 \times 10^8$ N/m^2. Considering interacting surfaces in our molecular models (26.15 nm^2 for configurations A and B and 9.95 nm^2 for configuration C), our simulations predict a force per area unit of 9.31×10^8, 0.75×10^8, and 11.59×10^8 N/m^2, for configurations A, B, and C, respectively. Results for configurations A and C are in excellent agreement with the experimental value, especially for configuration A (a difference of ∼0.26%). The value for configuration B is very low with respect to experimental data showing that in-plane misorientation of silicate-rich surfaces of particle pairs affects adhesion forces.

To go further in the comparison with and validation against available experiments, we computed the Young's modulus from our simulation datapoints by evaluating the first derivative of mean force at the interparticle distance where mean force cancelled for each configuration:

$$E_{\text{X}} = \frac{D^{\text{X}}_{ij,0}}{S^{\text{X}}_{\text{int}}} \cdot \left| \frac{\partial \langle f(D_{ij}) \rangle}{\partial D_{ij}} \right|_{D_{ij}=D^{\text{X}}_{ij,0}} ; \text{where X} = \text{A, B, C.} \qquad (15)$$

$S^{\text{X}}_{\text{int}}$ is the interacting surface for configuration X. Here, we used the values $S^{\text{A}}_{\text{int}} = S^{\text{B}}_{\text{int}} \sim 26.15$ nm^2 and $S^{\text{C}}_{\text{int}} \sim 9.95$ nm^2. $D_{ij,0}$ is the distance between centers of mass of particles where the mean force is cancelled. In practice, we took the closest simulation point to zero mean force and we found ∼2.4, ∼2.45, and ∼3.92 nm for configurations A, B, and C, respectively. The first derivative of the mean force at $D_{ij,0}$ was obtained using the Lagrange interpolation polynomial method in combination with three mean force data points, which were those 2 points on either side of $D_{ij,0}$ and the data point at $D_{ij,0}$. We computed $|\partial \langle f(D_{ij}) \rangle / \partial D_{ij}|$ for configurations A, B, and C, respectively, and we got 460.19 J/m^2, 78.47 J/m^2, and 179.43 J/m^2. Using eq. (15), we found Young's moduli of $E_{\text{A}} = 42.28$ GPa, $E_{\text{B}} = 7.36$ GPa, $E_{\text{C}} = 70.69$ GPa. On one hand, experimental Young's modulus for the C-S-H phase was found in the range 19-28 GPa[56]. Our results are higher than experiments for configuration A (about 1.5 to 2.2 times higher) and for configuration C (about 2.5 to 3.7 times higher). Configuration B exhibits a value lower than experiments (about 2.6 to 3.8 times lower). On the other hand, previous simulation works on the C-S-H simulation cell (periodic boundary conditions approximating fully dense C-S-H equivalent to stiffness of one C-S-H particle) gave Young's modulus in the range 55-74 GPa[5,44,57,58]. While our values for configurations A and C are very close to the previous simulation results, configuration B is 7 to 10 times lower. Overall, our results show that misorientation of silica chains affects strongly mechanical properties of the C-S-H phase. Beyond the effect of the contact nature among colloidal particles, another source influencing our results on Young's moduli is the number of contact between particles. Here, we considered only two explicit particles instead of many particles (aggregate), while it is an important effect in order to properly capture mechanical properties of a C-S-H aggregate[56]. Furthermore, calculations were restricted to rather small particle volume fractions, $\phi = 0.06$, and small RH, 10%. Computations using more conventional conditions could refine our simulated Young's moduli and match better experiments.

In addition, we computed the tensile rupture strain for configurations A, B and C, using distances where we found minima of mean force and combining it with distances where mean forces cancelled (∼2.4 nm, ∼2.45 nm, and ∼3.92 nm, respectively). We found 4.17%, 0%, and 1.79% for configurations A, B, and C, which is in fair agreement, but slightly lower to what was previously found in simulations of fully dense C-S-H (∼5%)[22,24,44]. To break particle pairs, the biggest strain needed is for configuration A, then comes configuration C and B. Note that for configuration B, we found 0%. This is explained by the fact that the closest point to the distance where the mean force is cancelled (i.e., our approximation of the mean force cancellation distance) corresponds also to the minimum of force.

Finally, mean forces are very close to 0 at long-range for configuration C, but there is non-negligible positive forces (repulsive) at long-range for configurations A and C. Looking at different contributions on the z-component of mean forces (Tab. 1 and Fig. 5 in Supporting Information), we observed that these positive values come mainly from C_w-particle interaction forces. We have checked with the help of cumulative charge density curves (see Fig. 3 in Supporting Information) that this is not the result of an unbalance of density of charges on each side of the particle. Indeed, it could give rise to a dipole moment affecting forces between particles. Half of the charge density of each contribution (i.e., water molecules, calcium counterions, and particle (*Si*, *O*, and *Ca* atoms)) is reached at the center of mass of each particle denoting a good balance of charges.

3.2 Interaction grand potentials

We constructed interaction grand potentials as a function of particle separation by applying equation (14) to the data given in Fig. 3; these profiles are shown in Fig. 4 as simulated points calculated for discrete values of D_{ij}, and are the basis of interaction grand potentials. Although previous reports of atomistically simulated forces and energy profiles between opposing surfaces (e.g., silica nanoplatelets[37], graphitelike nanoplatelets[65], and carbon nanotubes[66]) or molecules (e.g., methane-methane association[53]) noted oscillations in the energy profile attributed to molecular-scale features of confined water, such oscillations are not observed within the present profiles for C-S-H particle pairs. In fact, a detailed analysis of interaction grand potentials taking separately each contribution (i.e., water-particle, calcium counterion-particle, particle-particle, and the grand canonical term) showed that oscillations due to water are present but anihilated by the grand canonical term contribution in total interaction grand potentials (see Fig. 4 in Supporting Information).

Interaction grand potential minima appear at $D^{\text{A}}_{ij,\text{min}} \sim 2.28$ nm

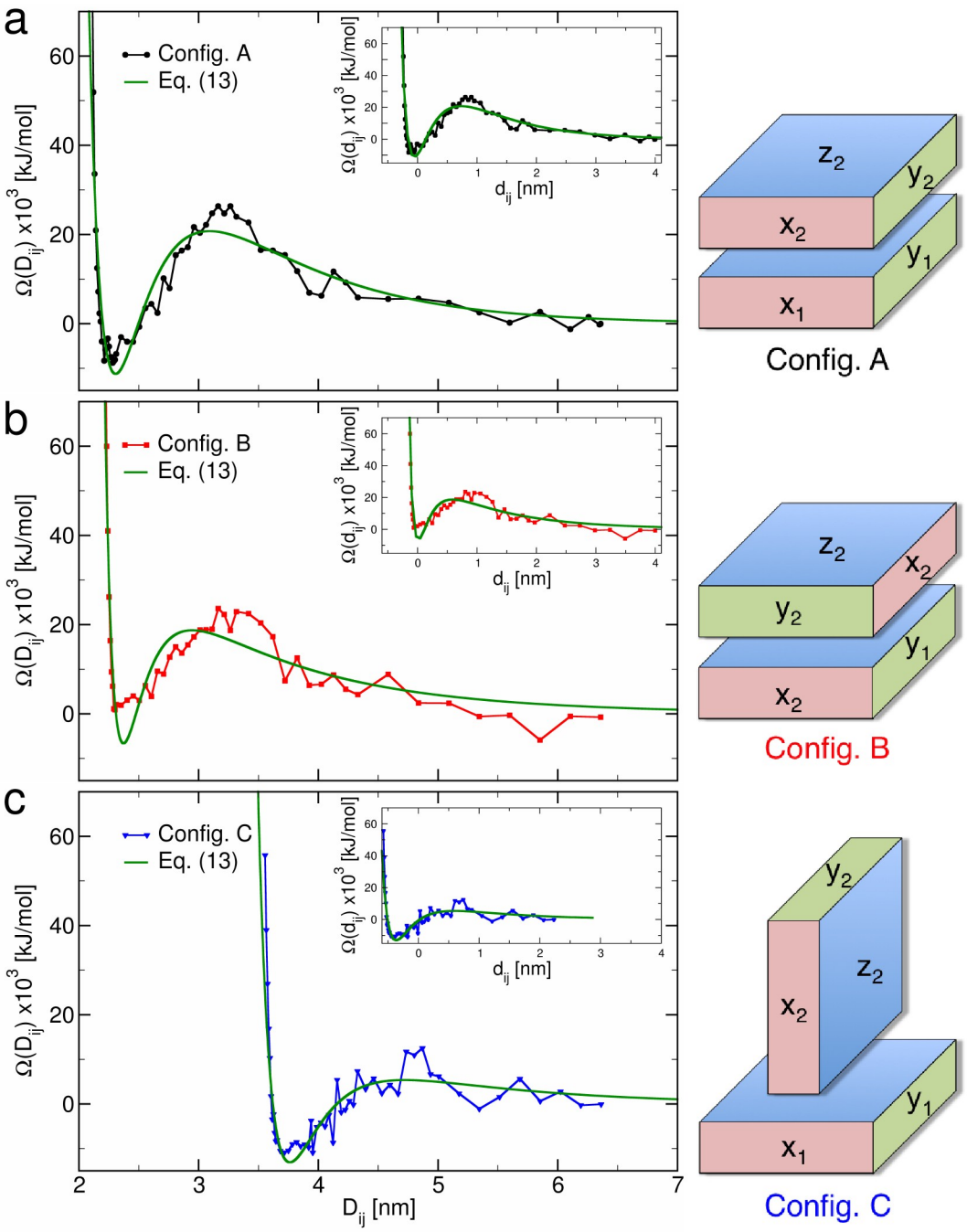

Fig. 4 Interaction grand potentials computed by integration of mean force for calcium-silicate-hydrate particles. Three configurations are investigated: (a) configuration A with black filled circles, (b) configuration B with red filled squares, and (c) configuration C with blue filled down triangles. Molecular details of these configurations can be found in Fig. 1 and cartoons are shown on the right side of the figure. $\{x_1, y_1, z_1\}$ and $\{x_2, y_2, z_2\}$ refer to surface normals for particle 1 (bottom) and particle 2 (top), respectively. Green solid lines stand for the pair potential energy curves obtained from the fitting of our simulation data with eq. (16). Insets show results as a function of d_{ij}, the distance between opposing free surfaces.

for configurations A and $D^{\mathrm{B}}_{ij,\mathrm{min}} \sim 2.30$ nm for configurations B, while for configuration C the minimum appears at a larger interparticle distance ($D^{\mathrm{C}}_{ij,\mathrm{min}} \sim 3.72$ nm). Again, this is due to the c_{part}:a_{part} particle aspect ratio that reduces the gap between particle pairs for the same distance D_{ij} when particle 2 is rotated as in configuration C. As above, we show in insets in Fig. 4a-c the results as a function of d_{ij}, the distance between opposing free surfaces. Minima in interaction grand potentials were at $d_{ij} \lesssim 0$ nm, with the shortest interparticle distance corresponding to configuration C ($d_{ij} = 0$ is the theoretical location of surface contact between particle pairs). Furthermore, we also observed local maxima (bumps) at $D^{\mathrm{A}}_{ij,\mathrm{bump}} \sim 3.16$ nm, $D^{\mathrm{B}}_{ij,\mathrm{bump}} \sim 3.16$ nm, and $D^{\mathrm{C}}_{ij,\mathrm{bump}} \sim 4.87$ nm with related interaction grand potentials of $\Omega^{A}_{\mathrm{bump}} \sim 26.34 \times 10^3$ kJ/mol, $\Omega^{B}_{\mathrm{bump}} \sim 23.59 \times 10^3$ kJ/mol, and $\Omega^{C}_{\mathrm{bump}} \sim 12.50 \times 10^3$ kJ/mol for configurations A, B, and C, respectively. These local maxima occur at distances where we previously found water content maxima and energy minima indicating that the interaction grand potential behavior is mainly driven by the water content (grand canonical contribution; second term in the right-hand side of eq. (14)). This statement is supported by Fig. 4 in Supporting Information, which shows the different quantities contributing to the interaction grand potential (i.e., water-particle, calcium counterion-particle, particle-particle, and grand canonical contributions). Therefore, changing the relative humidity will change the position of local maxima and their magnitude; since the interparticle distance D_{ij} at which water will condensate between particles will change. At 100% RH, this energy barrier will completely disappear, as a result of the expected small variations in water content with particle separation. The second term in the right-hand side of eq. (14) is expected to cancel out or at least to be negligible. Nevertheless, structural effects may appear at small particle separations, $D_{ij} < 1$ nm, due to the molecular nature of liquid water surrounding particles.

In order to state which configuration is the most prevalent and the most cohesive, we considered first the well-depths of interaction grand potentials for configurations A ($\Omega^{A}_{\mathrm{min}} \sim -8.81 \times 10^3$ kJ/mol), B ($\Omega^{B}_{\mathrm{min}} \sim 0.91 \times 10^3$ kJ/mol) and C ($\Omega^{C}_{\mathrm{min}} \sim -10.88 \times 10^3$ kJ/mol). This comparison shows that configuration C exhibits the strongest interparticle cohesion, followed by configuration A and then configuration B. If this finding shows the most cohesive of the three formed configurations, it does not consider the probability of formation (pairing) or breaking (unpairing) particle pairs, i.e., their stability. Usually, standard models are based on energy barriers computed from energy profiles freed from entropic effects ($-TS$) [67], i.e., the Free energy in the canonical ensemble and the interaction grand potential in the grand canonical ensemble (our work). Thus, we defined the energy barrier to form a particle pair as $\Delta\Omega_{\mathrm{form}} = \Omega(D_{\mathrm{bump}}) - \Omega(D_{\mathrm{max}})$ and the energy barrier to break a particle pair as $\Delta\Omega_{\mathrm{break}} = \Omega(D_{\mathrm{bump}}) - \Omega(D_{\mathrm{min}})$. Data are reported in Tab. 3. On one hand, configuration C will form faster than other configurations (highest probability of formation), since its energy barrier is about 50% lower that configurations B and A. Energy barriers for the two previous configurations are very similar (values within ~8%), meaning that the rate of formation for these two configurations is nearly the same. On the other hand, the highest energy barrier to break particle pairs is for configuration A followed by configuration C and B. Thus, energy well-depths and energy barriers show that configuration B is the least cohesive and the least stable configuration as depicted by its low rate of formation and its high rate of unpairing (lowest $\Delta\Omega_{\mathrm{break}}$). Configuration C, which is the most cohesive configuration (lowest energy well-depth), exhibit also a high rate of formation (lowest energy barrrier, $\Delta\Omega_{\mathrm{form}}$). However, its rate of breaking is also very high (one of the lowest energy barrrier, $\Delta\Omega_{\mathrm{break}}$), making configuration C not the most stable among other configurations. Configuration A is slightly less cohesive ($\Omega^{A}_{\mathrm{min}} < \Omega^{C}_{\mathrm{min}}$) and has also a lower rate of formation ($\Delta\Omega^{A}_{\mathrm{form}} > \Delta\Omega^{C}_{\mathrm{form}}$) with respect to configuration C. However, once formed, configuration A has less chances to break as depicted by the highest energy barrier with respect to other configurations. To resume, configuration A has the highest probability to be found among the configurations we explored, since it is the most stable. Our results further show that silicate chain misorientation for the same interacting surface area significantly affects the particle cohesion and stability (see results for configurations A and B). Not surprisingly, particles are found to be more cohesive when well aligned with silicate chains parallel to each other (configuration A), which corresponds essentially to a continuation of the C-S-H unit (stacking of C-S-H layers) or a growing C-S-H crystal. The high energy barrier found for the breaking process ensures its stability. Configuration B includes a stacking fault that significantly reduces interparticle cohesion and stability. These findings are in agreement with previous AFM results of Garrault et al.[2] on C-S-H growth on alite surfaces (C_3S in the cement industry notation), where they found that small elements of $60 \times 30 \times 5$ nm^3 in size (presumably C-S-H particles) exhibit silicate-rich layers oriented parallel to the surface. In that work, the particles were observed to aggregate against the alite surface such that silicate-rich layers of nanoparticles were aligned parallel to the alite surface (as in our configurations A). Garrault et al.'s observations could not distinguish between these two in-plane misorientations A and B, and also showed no evidence for configuration C, in which silicate layers would have been oriented perpendicular to alite. This observation is consistent with our finding that configuration A is one of the most energetically favored and the most stable.

3.3 Up-scaling data for mesoscale simulations

Interaction grand potentials shown in Fig. 4 look very similar to effective interaction potentials used at the mesoscale by Ioannidou et al.[21]. Nevertheless, one has to keep in mind that Ioannidou et al. approach[21] was developped to study the formation of C-S-H phase resulting in thermodynamic conditions different from our work (300 K and liquid water, 100% RH). Here, we defined a relative humidity of 10%, meaning that only a water layer is surrounding our molecular models of particles (conditions occuring for mature cement paste in extreme conditions). In Ioannidou et al. approach[21], the model used for pair interactions is a combination of a generalized Lennard-Jones potential and a

Table 3 Energy barriers extracted from interaction grand potentials.

Configuration	$\Delta\Omega_{\text{form}} \times 10^3$ [kJ/mol]	$\Delta\Omega_{\text{break}} \times 10^3$ [kJ/mol]
A	26.36	35.15
B	24.34	22.68
C	12.59	23.38

Yukawa repulsion:

$$U_{ij}(D_{ij}) = 4\varepsilon_{ij}\left[\left(\frac{\sigma_{ij}}{D_{ij}}\right)^{2\alpha} - \left(\frac{\sigma_{ij}}{D_{ij}}\right)^{\alpha}\right] + \psi_{ij}\sigma_{ij}\frac{\exp(-\sigma_{ij}(D_{ij}/\sigma_{ij}-1)/\lambda_{D,ij})}{D_{ij}}, \quad (16)$$

where σ_{ij} is the distance for which $U_{ij}(\sigma_{ij}) = 0$; ε_{ij} is the potential well-depth; α is the exponent in the generalized Lennard-Jones potential; ψ_{ij} is the energy of the Yukawa potential term when particle pairs are in contact ($D_{ij} = \sigma_{ij}$); and $\lambda_{D,ij}$ is the Debye screening length[21,68]. Eq. (16) was used to render our interaction grand potentials computed from atomistic simulations as useful input for mesoscale simulations. Fitting parameters are summarized in Table 4 and the resulting curves of the form of Eq. (16) shown in green in Fig. 4.

From fitting results, we found $\alpha \sim 7.24$, $\alpha \sim 13.01$, and $\alpha \sim 13.93$ for configurations A, B, and C, respectively. For configuration A, it is ∼1.66 times lower than the value used in Ioannidou et al. work[21], $\alpha = 12$. For configurations B and C, we got values ∼1.08 and ∼1.16 times higher. Since Ioannidou et al. particles are spherical in shape (isotropic), the value of 12 is an averge value of the different possible configurations between particle pairs. Averaging our fitted values, we found $\bar{\alpha} \sim 11.39$, which is close to the previous value. Regarding the Debye screening length λ_D, Ioannidou et al. considered a value corresponding to half of the particle diameter (0.5σ). Dividing our values of λ_D by their related σ, we found 0.56, 0.76, and 0.40 for configurations A, B, and C, respectively. Our molecular simulation values are in good agreement with the mesoscale model of Ioannidou et al.[21] despite different thermodynamic conditions (our work 300 K and 10%RH; Ioannidou et al. liquid water).

Interaction grand potential minima of our fitting curves with eq. (16) for configurations A, B, and C, are located at ∼2.31 nm, ∼2.37 nm, and ∼3.76 nm, respectively, which is in between 1.1% and 3.1% of simulated values, the least agreement being for configuration B. Related interaction grand potential minima are -11.26×10^3, -6.62×10^3, and -13.09×10^3 kJ/mol. This is within 30% of simulation values for configurations A and C. For configuration B, result of the fit gives a negative value for the potential well-depth, while the simulation value is positive. For that configuration, our fit of simulation data did not succeed in reproducing the well-depth. As a consequence, the cohesive property is not well reproduced by the generalized Lennard-Jones-Yukawa-type model for the interaction grand potential, for one of the three configurations considered. Nevertheless, the order is kept, since configuration C stay the most cohesive followed by configurations A and B. Locations of local maxima (bumps) are at 3.09 nm, 2.94 nm, and 4.72 nm for configuration A, B, and C, respectively. Previous values are between 2% and 7% of simulation results. Corresponding energies are found to be $\sim 20.74 \times 10^3$, $\sim 18.72 \times 10^3$, and $\sim 5.36 \times 10^3$ kJ/mol, which is ∼21% lower than simulation values for configurations A and B and ∼57% lower for configuration C. The least agreement found for configuration C can be chiefly attributable to appreciable fluctuations of the interaction grand potential in the region of the energy local maximum. Increased sampling of the reaction path in this region, by computing additional simulation points, may reduce these fluctuations and improve accuracy of the fitted curve around the local energy maximum, but would increase significantly the computational cost to obtain the interaction grand potential at each point.

Finally, to use these fits of interaction grand potentials as inputs for mesoscale simulations, one should consider the local relative orientation of interacting particles. Considering local axes of particles as defined in Fig.1, we suggest implementation of the interaction grand potentials derived here according to the following conditions:

$$\Omega(D_{ij}) = \begin{cases} \Omega^A(D_{ij}), \text{ if } |\overrightarrow{O_1x_1}\cdot\overrightarrow{O_2x_2}| > \frac{\sqrt{3}}{2} \text{ and } |\overrightarrow{O_1z_1}\cdot\overrightarrow{O_2z_2}| > \frac{\sqrt{3}}{2}; \\ \Omega^B(D_{ij}), \text{ if } |\overrightarrow{O_1x_1}\cdot\overrightarrow{O_2y_2}| > \frac{\sqrt{3}}{2} \text{ and } |\overrightarrow{O_1z_1}\cdot\overrightarrow{O_2z_2}| > \frac{\sqrt{3}}{2}; \\ \Omega^C(D_{ij}), \text{ if } |\overrightarrow{O_1y_1}\cdot\overrightarrow{O_2z_2}| > \frac{\sqrt{3}}{2} \text{ and } |\overrightarrow{O_1z_1}\cdot\overrightarrow{O_2y_2}| > \frac{\sqrt{3}}{2}, \end{cases}$$

where a deviation of 30° with respect to the alignment of local axes of particles is allowed. When possible, use of the interaction grand potential as interpolation among discrete simulated points is preferable to more accurately capture the particle interactions due to discrepancies in fits of the generalized Lennard-Jones-Yukawa type model to $\Omega(D_{ij})$.

4 Summary and outlook

In summary, we employed grand canonical Monte Carlo simulations to investigate mean forces between calcium-silicate-hydrate nanoparticles for defined physical environments (temperature and humidity), particle compositions, particle orientations, and particle volume fractions. Interaction grand potentials obtained with a mean force integration method are amenable for use in mesoscale simulations that describe cementitious materials at coarser length scales. These concepts are relevant to our ongoing efforts to predict computationally and improve the chemical, physical, and mechanical properties as well as the durability of cement.

The original scope of this work was to provide molecular-scale inputs that can be used to refine previous mesoscale simulations

Table 4 Fitting parameters used to model our interaction grand potentials obtained from mean force integration.

Configuration	$\varepsilon_{ij} \times 10^3$ [kJ/mol]	σ_{ij} [nm]	α	$\psi_{ij} \times 10^3$ [kJ/mol]	$\lambda_{D,ij}$ [nm]
A	140.91	2.02	7.24	179.34	1.13
B	48.49	2.23	13.01	47.81	1.70
C	32.63	3.56	13.93	23.59	1.42

of cement pastes that showed nucleation and growth of C-S-H nanoparticles[69], the C-S-H phase formation[21], and the effect of the volume fraction (or packing density) on mechanical properties[22,24]. In the work of Masoero et al., C-S-H particles were idealized as isotropes (spheres), and interaction potentials between these C-S-H particles were assumed, simple functional forms that were independent of the volume fraction and the physical environment. An improvement to such interaction potentials was found in the work of Ioannidou et al., where characteristics of interactions depend on the environment, including features such as solution ionic strength, pH and temperature. Nevertheless, that study did not account for effects of particle density, the molecular nature of water relevant to small interparticle distances, or geometric anisotropy of particles on the interaction potentials. Here, we provide molecular-scale based interaction grand potentials including the effect of density of particles and the environment that could serve as effective potentials among particles in such mesoscale simulations, for systems with a volume fraction of $\phi \sim 0.06$ at room temperature (300 K) and at low relative humidity (10%RH).

Under the physical conditions assumed to illustrate these methods, we had not found oscillations originating from the structuration of the solvent in interaction grand potentials due to the significant contribution of the grand canonical term. Furthermore, we found that cohesion between particles is affected strongly by both the particle dimensions and crystallographic misorientation of interacting nanoparticles. Finally, we fitted our data with a generalized Lennard-Jones-Yukawa type potential and provided criteria for using such descriptions of particle interactions at the mesoscale.

Although the conditions considered herein were distinct from humidities and particle volume fractions relevant to many hardened cement pastes (300 K, 50-60%RH, $0.64 < \phi < 0.74$) or to C-S-H formation (approaching 100%RH), the conceptual and computational approach described can be used now for a wider range of environments. Further, the low humidity case we document here can be relevant to either extremely arid environments or related to those at high temperatures that promote water desorption from the porous network. The approximation of interaction grand potentials with compact mathematical forms for effective potentials can also be adapted (e.g., via configurations that facilitate fitting to a Gay-Berne potential[70]). Overall, this approach provides a novel and tractable means to consider how aqueous solution chemistry (water, ions), particle composition, and particle volume fraction affect forces between calcium-silicate-hydrate nanoparticles (or surfaces) at the molecular scale and, thus to predict the overall chemomechanical properties of cement at the meso- and macroscales.

Acknowledgements

The authors thank H. Jennings, E. Masoero and A. Nonat for fruitful discussions. K. J. Van Vliet and P. A. Bonnaud acknowledge partial funding from the MIT Concrete Sustainability Hub, supported by the Portland Cement Association and National Ready Mix Concrete Association.

References

1 S. Gauffinet, E. Finot, E. Lesniewska and A. Nonat, *Comptes rendus de l'Académie des Sci., Série 2, Sciences de la terre et des Planètes*, 1998.

2 S. Garrault, E. Finot, E. Leniewska and A. Nonat, *Materials and Structures*, 2005, **38**, 435–442.

3 K. J. Van Vliet, R. J.-M. Pellenq, M. J. Buehler, J. C. Grossman, H. Jennings, F.-J. Ulm and S. Yip, *MRS Bulletin*, 2012, **37**, 395–402.

4 N. Tanaka and B. Stigson, *Cement Technology Roadmap 2009*, World business council for sustainable development and the international energy agency technical report, 2009.

5 H. Manzano, J. S. Dolado and A. Ayuela, *Acta Materialia*, 2009, **57**, 1666–1674.

6 L. Nachbaur, J. C. Mutin, A. Nonat and L. Choplin, *Cement and Concrete Research*, 2001, **31 (2)**, 183–192.

7 C. Plassard, E. Leniewska, I. Pochard and A. Nonat, *Langmuir*, 2005, **21 (16)**, 7263–7270.

8 B. Jönsson, A. Nonat, C. Labbez, B. Cabane, and H. Wennerström, *Langmuir*, 2005, **21 (20)**, 9211?9221.

9 H. F. W. Taylor, *Cement Chemistry*, Academic press., 1997, p. 475.

10 S. Garrault and A. Nonat, *Langmuir*, 2001, **17**, 8131–8138.

11 I. G. Richardson, *Cement and Concrete Research*, 1999, **29**, 1131.

12 A. Nonat, *Cement and Concrete Research*, 2004, **34 (9)**, 1521–1528.

13 G. Kovačević, B. Persson, L. Nicoleau, A. Nonat and V. Veryazov, *Cement and Concrete Research*, 2015, **67**, 197–203.

14 C. Labbez, B. Jönsson, I. Pochard, A. Nonat and B. Cabane, *The Journal of Physical Chemistry B*, 2006, **110 (18)**, 9219–9230.

15 H. M. Jennings, J. W. Bullard, J. J. Thomas, J. E. Andrade, J. J. Chen and G. W. Scherer, *Journal of Advanced Concrete Technology*, 2008, **6**, 5–29.

16 H. M. Jennings, *Cement and Concrete Research*, 2008, **38**, 275–289.

17 A. J. Allen, J. J. Thomas and H. M. Jennings, *Nature Materials*, 2007, **6**, 311.

18 H. M. Jennings, J. J. Thomas, J. S. Gevrenov, G. Constantinides and F.-J. Ulm, *Cement and Concrete Research*, 2007, **37**, 329.

19 A. Gmira, M. Zabat, R. J.-M. Pellenq and H. V. Damme, *Materials and Structures*, 2004, **37**, 3.

20 L. Gatty, S. Bonnamy, A. Feylessoufi, C. Clinard, P. Richard and H. V. Damme, *Journal of Materials Science*, 2001, **36**, 4013.

21 K. Ioannidou, R. J.-M. Pellenq and E. D. Gado, *Soft Matter*, 2014, **10**, 1121–1133.

22 E. Masoero, E. D. Gado, R. J.-M. Pellenq, F.-J. Ulm and S. Yip, *Physical Review Letters*, 2012, **109**, 155503.

23 A. Thuresson, M. Ullner, T. Åkesson, C. Labbez and B. Jönsson, *Langmuir*, 2013,

29 (29), 9216–9223.

24 E. Masoero, E. D. Gado, R. J.-M. Pellenq, S. Yip and F.-J. Ulm, *Soft Matter*, 2014,

14 | 1 1–14

25 M. Turesson, A. Nonat and C. Labbez, *Langmuir*, 2014, **30 (23)**, 6713?6720.

26 J. N. Israelachvili and G. E. Adams, *Journal of the Chemical Society, Faraday Transaction 1: Physical Chemistry in Condensed Phases*, 1978, **74**, 975–1001.

27 R. G. Horn and J. N. Israelachvili, *Journal of Chemical Physics*, 1981, **75**, 1400.

28 J. N. Israelachvili and H. K. Christenson, *Physica*, 1986, **140A**, 278–284.

29 J. Israelachvili, *Intermolecular and Surface Forces*, Academic Press, 2nd edn., 1991.

30 E. J. W. Verwey and J. T. G. Overbeek, *Theory of the Stability of Lyophobic Colloids*, Elsevier, Amsterdam, 1949.

31 J. T. G. Overbeek, *General Discussions, Discussions Faraday Society*, 1978.

32 B. Beresford-Smith and Y. C. Chan, *Chemical Physics Letters*, 1982, **92**, 474.

33 A. Agra, E. Trizac and L. Bocquet, *The European Physical Journal E*, 2004, **15**, 345:357.

34 M. Turesson, B. Jönsson and C. Labbez, *Langmuir*, 2012, **28**, 4926–4930.

35 C. Labbez, I. Pochard, B. Jonsson and A. Nonat, *Cement and Concrete Research*, 2011, **41**, 161.

36 R. J.-M. Pellenq, *L'Actualité Chimique*, 2004, **273**, 12–22.

37 T.-D. Li, J. Gao, R. Szoszkiewicz, U. Landman and E. Riedo, *Physical Review B*, 2007, **75**, 115415.

38 S. Leroch and M. Wendland, *The Journal of Physical Chemistry C*, 2012, **116**, 26247–26261.

39 S. Leroch and M. Wendland, *Langmuir*, 2013, **29**, 12410.

40 R. T. Cygan, J. A. Greathouse, H. Heinz and A. G. Kalinichev, *Journal of Materials Chemistry*, 2009, **19**, 2470–2481.

41 D. Ebrahimi, A. J. Whittle and R. J.-M. Pellenq, *Journal of Chemical Physics*, 2014, **140**, 154309.

42 P. Bonnaud, Q. Ji, B. Coasne, R. J.-M. Pellenq and K. J. V. Vliet, *Langmuir*, 2012, **28**, 11422.

43 P. Bonnaud, Q. Ji and K. J. V. Vliet, *Soft Matter*, 2013, **9**, 6418–6429.

44 R.-M. Pellenq, A. Kushima, R. Shahsavari, K. J. V. Vliet, M. J. Buehler, S. Yip and F.-J. Ulm, *Proceeding of the National Academy of Sciences*, 2009, **106**, 16102.

45 Q. Ji, R. J.-M. Pellenq and K. J. V. Vliet, *Computational Materials Science*, 2012, **53**, 234–240.

46 G. Groves, P. J. L. Sueur and W. Sinclair, *Journal of the American Ceramic Society*, 1986, **69**, 353.

47 I. G. Richardson and G. W. Groves, *Journal of Materials Science*, 1992, **27**, 6204–6212.

48 M. J. DeJong and F.-J. Ulm, *Cement and Concrete Research*, 2007, **37**, 1–12.

49 R. J.-M. Pellenq and D. Nicholson, *Journal of Physical Chemistry*, 1994, **98**, 13339.

50 H. J. C. Berendsen, J. *molecular Forces*, ed. B. Pullman, Reidel, Dordrecht, 1981, p. 331.

51 D. Frenkel and B. Smit, *Understanding Molecular Simulation: From Algorithms to Applications*, 2nd Ed., Academic Press, London, 2002.

52 J. Vorholz, V. I. Harismiadis, B. Rumpf, A. Z. Panagiotopoulos and G. Maurer, *Fluid Phase Equilibria*, 2000, **107**, 203.

53 D. Trzesniak, A.-P. E. Kunz and W. F. van Gunsteren, *ChemPhysChem*, 2007, **8**, 162–169.

54 M. Deserno and C. Holm, *The Journal of Chemical Physics*, 1998, **109**, 7678–7693.

55 W. Smith and T. R. Forester, *Journal of Molecular Graphics*, 1996, **14 (3)**, 136–141.

56 G. Constantinides and F.-J. Ulm, *Cement and Concrete Research*, 2004, **34**, 67–80.

57 H. Manzano, J. S. Dolado, A. Guerrero and A. Ayuela, *Physica Status Solidi (a)*, 2007, **204**, 1775–1780.

58 H. Manzano, S. Moeini, F. Marinelli, A. C. T. van Duin, F.-J. Ulm and R. J.-M. Pellenq, *Journal of the American Chemical Society*, 2012, **134**, 2208–2215.

59 G. Constantinides and F.-J. Ulm, *Journal of the Mechanics and Physics of Solids*, 2007, **55**, 64–90.

60 M. Vandamme and F.-J. Ulm, *Proceeding of the National Academy of Sciences*, 2009, **106 (26)**, 10552–10557.

61 T. C. Powers and T. L. Brownyard, Research Laboratories of the Portland Cement Association Bull. 22, 1948.

62 R. F. Feldman and P. J. Sereda, *Engineering Journal*, 1970, **53 (8-9)**, 53–59.

63 R. F. Feldman, P. J. Sereda and V. S. Ramachandran, 7th International Congress on the Chemistry of Cement, Paris, 1980, pp. VI.1/1–VI.1/36.

64 R. Sierra, *Bulletin de liaison du Laboratoire Centrale des Ponts et Chaussées*, 1982, **117**, 77–81.

65 N. Choudhury and B. Montgomery Pettitt, *Journal of the American Chemical Society*, 2005, **127**, 3556–3567.

66 N. M. Uddin, F. M. Capaldi and B. Farouk, *Polymer*, 2011, **52**, 288–296.

67 B. Rotenberg, V. Marry, R. Vuilleumier, N. Malikova, C. Simon and P. Turq, *Geochimica and Cosmochimica Acta*, 2007, **71**, 5089–5101.

68 A.-P. Hynninen and M. Dijkstra, *Journal of Physics: Condensed Matter*, 2003, **15**, S3557–S3567.

69 R. Gonzáles-teresa, J. S. Dolado, A. Ayuela and J.-C. Gimel, *Applied Physics Letters*, 2013, **103**, 234105.

70 R. A. X. Persson, *Journal of Chemical Physics*, 2012, **136**, 226101.